Article:
Zhao, Zhuo, Xu, Sheng, Wood, Bradford J et al. (2019) The Feasibility of Using a Smartphone Magnetometer for Assisting Needle Placement. Journal of biomedical optics. ISSN: 1560-2281

https://doi.org/10.1007/s10439-019-02436-5

Annals of Biomedical Engineering (© 2019)
https://doi.org/10.1007/s10439-019-02436-5

BMES BIOMEDICAL ENGINEERING SOCIETY

Original Article

The Feasibility of Using a Smartphone Magnetometer for Assisting Needle Placement

ZHUO ZHAO,[1] SHENG XU,[2] BRADFORD J. WOOD,[2] HONGLIANG REN,[3] and ZION TSZ HO TSE[1,4]

[1]School of Electrical and Computer Engineering, University of Georgia, Athens, GA, USA; [2]Center for Interventional Oncology, National Institutes of Health, Bethesda, MD, USA; [3]Department of Biomedical Engineering, National University of Singapore, Singapore, Singapore; and [4]College of Engineering, The University of Georgia, 597 D. W. Brooks Dr, Athens, GA 30602, USA

(*Received 20 July 2019; accepted 8 December 2019*)

Associate Editor Sean S. Kohles oversaw the review of this article.

Abstract—Minimally invasive surgical procedures often require needle insertion. For these procedures, efficacy greatly depends on precise needle placement. Many methods, such as optical tracking and electromagnetic tracking, have been applied to assist needle placement by tracking the real-time position information of the needle. Compared with the optical tracking method, electromagnetic tracking is more suitable for minimally invasive surgery since it has no requirement of line-of-sight. However, the devices needed for electromagnetic tracking are usually expensive, which will increase the cost of surgery. In this study, we presented a low-cost smartphone-based permanent magnet tracking method compatible with CT imaging and designed a 3D printed operation platform to assist with needle placement prior to needle insertion during minimally invasive surgery. The needle positioning accuracy of this method was tested in an open air test and a prostate phantom test in a CT environment. For these two tests, the average radial errors were 0.47 and 2.25 mm, respectively, and the standard deviations were 0.29 and 1.63, respectively. The materials and fabrication required for the presented method are inexpensive. Thus, many image-guided therapies may benefit from the presented method as a low-cost option for needle positioning prior to needle insertion.

Keywords—Magnet tracking, Smartphone, Needle placement.

INTRODUCTION

Needle insertion is one of the most common procedures in minimally invasive surgeries such as biopsy, fine-needle aspiration (FNA), brachytherapy, and thermal treatment or ablation.[1,16,17] During these procedures, accurate needle placement is very important in order to minimize the invasiveness to the patient and improve the clinical outcomes.[1,13,16,17,19,23] Currently, many imaging modalities, such as ultrasound (US), magnetic resonance imaging (MRI), and computed tomography (CT), are used for image guidance to improve the accuracy of needle placement, reduce complications, and shorten intervention time.[1,10] In addition, they can be combined with device tracking to locate the needle in real-time, thus improving the efficiency and accuracy of needle placement. Optical tracking and electromagnetic (EM) tracking are two localization methods widely used for this purpose.[10] Many researchers have reported studies on these methods, such as Black *et al.*,[5] who developed an optical tracking system with three light-emitting diodes located on a special needle holder for accurate needle placement. Gergel *et al.*[11] made an EM navigation system to track the location of a needle for accurate needle placement in transbronchial needle aspiration (TBNA) procedures. However, there are limitations with these systems. One drawback of optical tracking is the requirement of line-of-sight, which precludes it from being used in tracking internal targets. EM tracking also has downsides since it involves integrating wired tracking sensors with standard devices, which results in high disposable cost and increased sterilization and operation complexity.

In response to the above problems, we presented a method to use a permanent magnet for device tracking in minimally invasive procedures. Permanent magnet tracking is widely used in wearable devices and input

Address correspondence to and Zion Tsz Ho Tse, College of Engineering, The University of Georgia, 597 D. W. Brooks Dr, Athens, GA 30602, USA. Electronic mail: ziontse@uga.edu

Published online: 12 December 2019

devices. For example, Han *et al.*[12] applied this technique in a wearable handwriting input device for writing characters. Chen *et al.*[6] developed a 3D input system with two magnetometers. Yoon *et al.*,[24] Abdelnasser *et al.*,[3] Abe *et al.*,[4] Cheung and Girouard,[7] and Abdelnasser *et al.*[2] developed wireless input devices for smartphones based on the permanent magnet tracking. A smartphone has an integrated magnetometer and screen, making it a compact device for detecting magnetic fields and displaying tracking results. In this study we developed a smartphone-based permanent magnet tracking system for CT guided minimally invasive surgery. This approach does not require modification of standard needles and can significantly reduce the cost of needle navigation during surgery. Preliminary data was first reported as an oral presentation at the 2019 International Symposium on Medical Robotics as the proof of concept.[25] The goal of the presented method was to achieve a comparable localization accuracy and cost but higher resolution compared with the template approaches, which usually have a localization accuracy of around 3 mm, resolution of 2–5 mm,[9,18,21,22] and cost of $10–$30 per piece.

MATERIALS AND METHODS

The presented system consists of a magnet as signal emitter, a smartphone with magnetometer as a signal receiver, and a 3D printed platform to hold the magnet and smartphone during tracking procedure. The position of the magnet can be tracked in real-time based on a developed math model through measured values from the magnetometer on the smartphone. The magnet position is described in a CT scanner coordinate system with magnetometer as the origin and displayed on the smartphone screen to assist the operator for needle placement. All symbols used to develope the presented method are summarized in Table 1.

Math Model

The position relationship between the magnet and the smartphone's magnetometer in 3D space is shown in Fig. 1(a). It is assumed that the magnetic moment of the magnet (the South–North axis (S–N)) is in parallel with the y-axis in the given magnetometer coordinate system, and the parallel relationship does not change during movement. In calculation, the magnetic dipole model is applied, and the magnetometer is assumed as a point.

The relationship between the magnetic field and the position in a magnetic dipole model is shown in Eq. (1).[8]

$$\vec{B}(\vec{m},\vec{r}) = \frac{\mu_0}{4\pi|\vec{r}|^5}\left[3(\vec{r}\cdot\vec{m})\vec{r} - |\vec{r}|^2\vec{m}\right], \tag{1}$$

where $\vec{B}$ is the strength of the magnetic field, and it can be measured through a magnetometer in three axes and represented by (b_x, b_y, b_z); μ_0 is the vacuum permeability; $\vec{r}$ is the position of the magnet in the Cartesian coordinate system oriented by the magnetometer, and it can be represented by (x, y, z); and $\vec{m}$ is the magnetic moment of the magnet, and it can be represented by $(0, m, 0)$ based on our assumption. By replacing $\vec{B}$, $\vec{m}$, and $\vec{r}$, we can get three equations:

$$\begin{bmatrix} b_x \\ b_y \\ b_z \end{bmatrix} = \frac{\mu_0 m}{4\pi|\vec{r}|^5}\begin{bmatrix} 3yx \\ 3y^2 - |\vec{r}|^2 \\ 3yz \end{bmatrix}. \tag{2}$$

We assume the angle between the negative direction of the y-axis and $\vec{r}$ is θ, as shown in Fig. 1(a). Thus, Eq. (2) can be rewritten as follows:

$$\begin{bmatrix} b_x^2 + b_z^2 \\ b_y \end{bmatrix} = \begin{bmatrix} (3\sin\theta\cos\theta)^2 & 0 \\ 0 & 3\cos^2\theta - 1 \end{bmatrix}\begin{bmatrix} \left(\frac{\mu_0 m}{4\pi|\vec{r}|^3}\right)^2 \\ \frac{\mu_0 m}{4\pi|\vec{r}|^3} \end{bmatrix} \tag{3}$$

TABLE 1. Symbols used in paper.

Symbol	Definition
$\vec{B}$	Strength of magnetic field
b_x	Measured x-axis strength of magnetic field from magnetometer
b_y	Measured y-axis strength of magnetic field from magnetometer
b_z	Measured z-axis strength of magnetic field from magnetometer
μ_0	Vacuum permeability
$\vec{r}$	Distance vector from sensor to magnet
$\vec{m}$	Magnetic moment
θ	The angle between negative direction of y-axis and $\vec{r}$
$\hat{x}_{n\|m}$	The estimate of x at time n given observations up to and including at time $m \le n$
$P_{n\|m}$	The posteriori error covariance matrix corresponding to $\hat{x}_{n\|m}$
F_k	The state-transition model
B_k	The control-input model
u_k	Control vector
Q_k	The covariance of the process noise
K_k	The optimal Kalman gain
H_k	The observation model which maps the true state space into the observed space
z_k	The observation of the true state x_k at time k
R_k	The covariance of the observation noise
I	Unit matrix
H_k^T	Transpose of matrix H_k

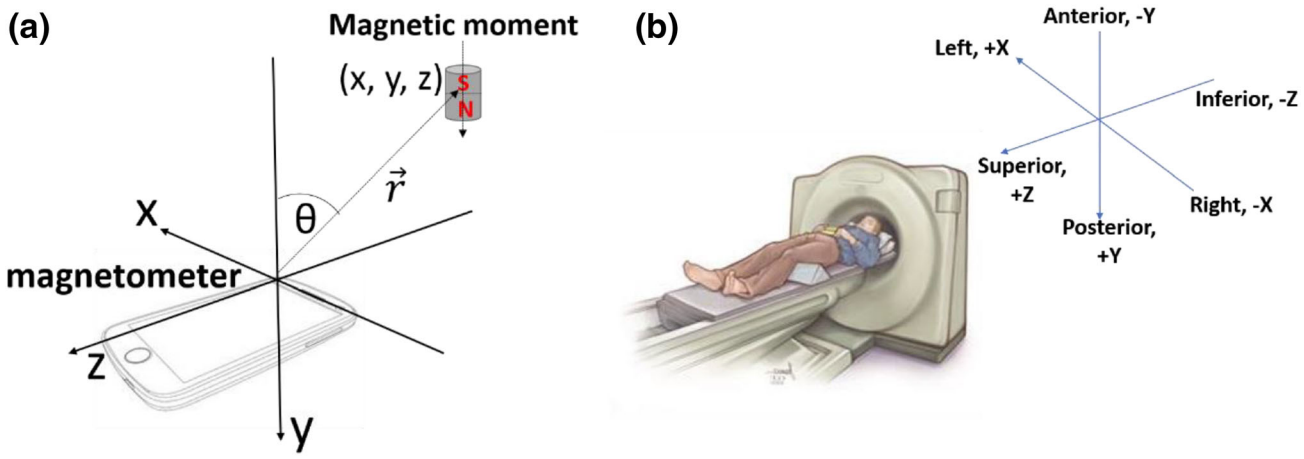

FIGURE 1. Illustrations of (a) the coordinate system of a smartphone, and the position relationship between the magnet and magnetometer in 3D space, (b) the coordinate system of a CT scanner.

The double angle formula is then applied to Eq. (3), so we can get a quadratic equation about $|\vec{r}|^3$. By solving this equation, we can get

$$|\vec{r}|^3 = \frac{\mu_0 m}{4\pi} K, \tag{4}$$

where $K = \frac{b_y + \sqrt{9b_y^2 + 8\left(b_x^2 + b_z^2\right)}}{2\left(b_x^2 + b_y^2 + b_z^2\right)}$. By substituting Eq. (4) into (2), we can solve for y^2:

$$y^2 = \frac{1}{3}\left(\frac{\mu_0 m}{4\pi}\right)^{\frac{2}{3}} \left(b_y K^{\frac{5}{3}} + K^{\frac{2}{3}}\right). \tag{5}$$

In this application, the working area is in the negative direction of the y-axis. Thus,

$$y = \frac{-1}{\sqrt{3}}\left(\frac{\mu_0 m}{4\pi}\right)^{\frac{1}{3}} K^{\frac{1}{3}} \sqrt{b_y K + 1}. \tag{6}$$

By substituting Eq. (6) into (2), we can solve x and z. The final solution for x, y, and z in our working area is:

$$\begin{bmatrix} x \\ y \\ z \end{bmatrix} = \frac{-1}{\sqrt{3}}\left(\frac{\mu_0 m}{4\pi}\right)^{\frac{1}{3}} \begin{bmatrix} \frac{K^{\frac{4}{3}} b_x}{\sqrt{b_y K + 1}} \\ K^{\frac{1}{3}}\sqrt{b_y K + 1} \\ \frac{K^{\frac{4}{3}} b_z}{\sqrt{b_y K + 1}} \end{bmatrix}. \tag{7}$$

In Eq. (7), the magnetic moment m is a constant for a given magnet, and b_x, b_y, and b_z can be measured through a magnetometer. Therefore, we can get the position information of the magnet via a magnetometer-oriented coordinate system based on Eq. (7).

Filter

A filter was applied to reduce noise and make the output signal of the magnetometer smoother. In total, four filters were compared: first-order low pass filter, second-order low pass filter, moving average filter, and Kalman filter. We found that the Kalman filter had the best performance, so in our program, we used the Kalman filter to reduce noise.

The Kalman filter uses a series of measurements observed over time and produces estimates of unknown variables. It is most often calculated as two distinct phases: "Predict" and "Update." In the predict phase, which is also called the *priori* state estimate, it uses the state estimate from the previous timestep to produce an estimate of the state at the current timestep. The *priori* state estimate and the estimate covariance are predicted in this phase, as shown in Eqs. (8) and (9), respectively[15,20]:

$$\hat{x}_{k|k-1} = F_k \hat{x}_{k-1|k-1} + B_k u_k, \tag{8}$$

$$P_{k|k-1} = F_k P_{k|k-1} F_k^T + Q_k, \tag{9}$$

where $\hat{x}_{n|m}$ represents the estimate of x at time n given observations up to and including at time $m \le n$, $P_{n|m}$ represents the posteriori error covariance matrix corresponding to $\hat{x}_{n|m}$, F_k is the state-transition model, B_k is the control-input model, u_k is the control vector, and Q_k is the covariance of the process noise.

The current *priori* prediction is combined with the current observation information to refine the state estimate in the update phase, which is also known as the posteriori state estimate. In this phase, it will up-

date the posteriori state estimate, optimal Kalman gain, and the posteriori estimate covariance, as shown from Eqs. (10) through (12), respectively[15,20]:

$$\hat{x}_{k|k} = \hat{x}_{k|k-1} + K_k\left(z_k - H_k\hat{x}_{k|k-1}\right), \tag{10}$$

where K_k is the optimal Kalman gain, H_k is the observation model which maps the true state space into the observed space, and z_k is the observation of the true state x_k at time k.

$$K_k = P_{k|k-1}H_k^T\left(R_k + H_kP_{k|k-1}H_k^T\right)^{-1}, \tag{11}$$

where R_k is the covariance of the observation noise.

$$P_{k|k} = (I - K_kH_k)P_{k|k-1}, \tag{12}$$

where I is a unit matrix.

In this application, the strength of the magnetic field is a one-dimensional number in each axis, and the three axes of the magnetometer have similar physical processes, so we can use the same parameters for filtering the measured values from the three axes. Specifically, through tests, we set $R_k = 0.071$ in our program. Q_k is a parameter that can decide whether the optimal value is closer to the measured value or the value from the *priori* state estimate, so it is a dynamic value calculated based on the variability of the magnetic field as shown in Eqs. (13) and (14):

$$Q_k = log_{1.5}\Delta - 3.6, \tag{13}$$

$$\Delta = m_k - \hat{x}_{k-1|k-1}, \tag{14}$$

where m_k is the measured value at time k.

Program

The Android app was developed in App Inventor. Since a magnetic field can affect the calculation results from the math model, the program needs to collect magnetic field information from the surrounding environment first. Background noise can be reflected more accurately with more collections. However, more collections require more time. A balance between data size and number of collections needs to be found. In our case, we sampled the background magnetic baseline for 5 s at 40 Hz and used the average as the background noise. Then the difference between the tracking data and the background noise is considered as (b_x, b_y, b_z) when calculating the position of the magnet.

In addition, the constant $\left(\frac{\mu_0 m}{4\pi}\right)^{\frac{1}{3}}$ in the math model is hard to measure. Therefore, a calibration step was added to calculate this constant before tracking. In this step, the working plane (x–y, x–z, or y–z) is selected first, and each axis in the selected plane is calibrated independently. For each axis, the user inputs a known distance between two points, and the corresponding coordinate information of these two points is recorded with the assumption of $\left(\frac{\mu_0 m}{4\pi}\right)^{\frac{1}{3}} = 1$. Then we can get a calculated value of $\left(\frac{\mu_0 m}{4\pi}\right)^{\frac{1}{3}}$ by dividing the known distance by the absolute difference between the corresponding coordinate information of the two points. In the calibration step, we can get two calculated values of $\left(\frac{\mu_0 m}{4\pi}\right)^{\frac{1}{3}}$ from the selected axis calibration, and we then use the average of these two values as the final value of $\left(\frac{\mu_0 m}{4\pi}\right)^{\frac{1}{3}}$.

For the tracking function, the program always assumes the first tracked point as the original point and draws it in the center of the screen. Then, a 2D coordinate system is built based on this original point on the phone screen with the head and right side of the phone being the two position directions of the two axes. For the following points, the program uses the relative distance between the new point and the first tracked point as a reference for drawing. The workflow of the program is shown in Fig. 2.

Hardware Design

A platform was designed to make sure the magnetic moment of the magnet (i.e., the S–N axis) stays in parallel with one axis of the magnetometer, as shown

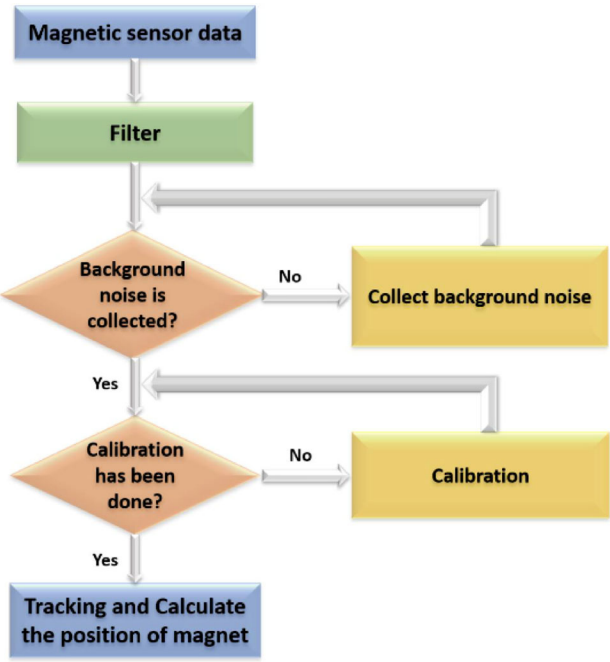

FIGURE 2. Illustration of software workflow in this application.

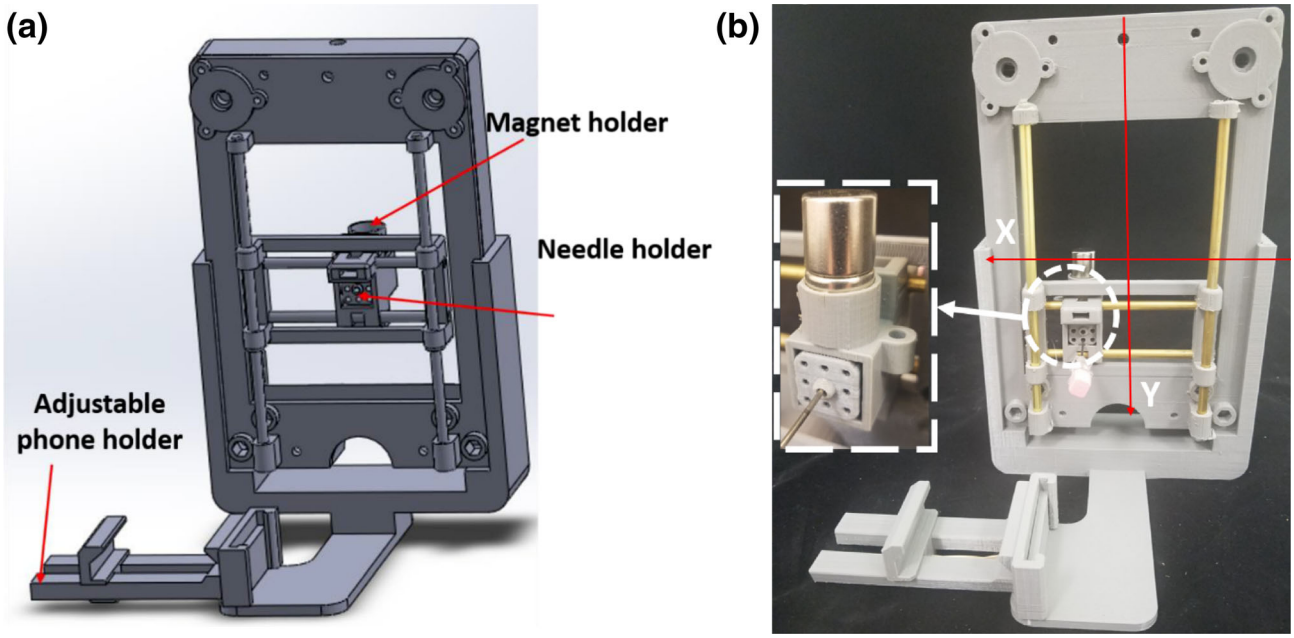

FIGURE 3. (a) 3D model of the operation platform. (b) 3D printed operation platform with a working plane in CT coordinate system.

in Fig. 3. This platform consisted of a needle insertion template, magnet holder, and adjustable phone holder. The needle insertion template is used for holding a needle during localization procedures, and it is connected with the magnetic holder to make sure it has the same movement distance as the tracked magnet. In addition, a brass tube was used as a slider bar for reducing the background noise of measurement and increasing the signal-to-noise ratio (SNR) captured by the magnetometer in the smartphone. Once the design was finalized, the platform was printed by a 3D printer (MakerBot, New York City, NY). The working area of this platform was the x-y plane in the CT coordinate system, as shown in Fig. 1. Besides, the size of the working area was calibrated based on the used magnet.

Two experiments were conducted to test the tracking accuracy of the tracking method presented in this paper. A Samsung S7 edge smartphone with an assembled magnetometer, which has a maximum measurement range of 4912 micro-Tesla (μT) and resolution of 0.60 μT, and a neodymium N52 magnet, which has a diameter of 14 mm and a height of 28 mm, were used in all experiments.

The strength of the magnetic field decreases significantly with the increase of distance between the magnetometer and magnet, which leads to a decrease of SNR and inaccurate tracking. Therefore, we needed to confirm the acceptable working area of the magnet based on the SNR before the experiment.

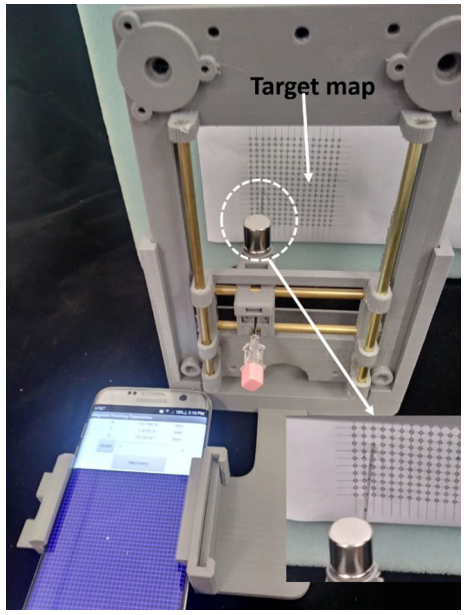

FIGURE 4. Experiment setup for an open-air test.

Working Area Measurement

To keep the magnet from getting too close to the magnetometer in the smartphone, the working area was started from the right edge of the smartphone. First, the magnetic field strength of the environment was recorded as background noise. Then the magnet was moved around in the space to the right of the

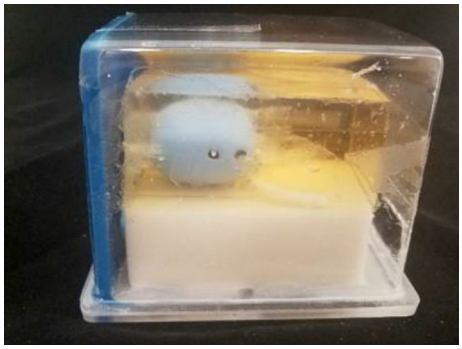

FIGURE 5. Prostate phantom used in this application (CIRS Inc., Norfolk, VA).

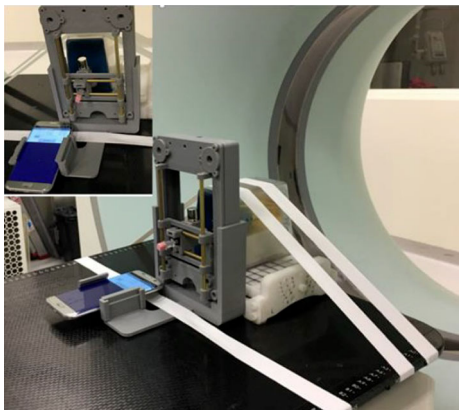

FIGURE 6. Experiment setup for prostate phantom tests.

smartphone, and the SNR was calculated during the movement of the magnet. The area with SNR greater than one could be considered as a potential working area. However, the background noise in the CT environment was greater than that in the lab environment, which means the same position will have a smaller SNR in a CT environment than an open-air environment. So, to make sure the working area can work in both open-air and CT environments, the area with SNR greater than 1.5 in the open-air environment was selected as the working area.

Open Air Test

A target map was created for the open-air test, and any two adjacent targets were separated by 5 mm. The experiment setup is shown in Fig. 4. During the test, the needle tip was placed on the center point of the target map first, which was recorded as the initial point. Then the needle tip was randomly moved to another point, and this point was recorded as the target point. The distance between the initial point and target point was calculated in two ways: (1) based on app measurement information and (2) based on the target map. The difference between these two distances was the tracking error. Twenty-five points were randomly selected on the target map for this test. In addition, the magnetometer was recalibrated through a figure-eight motion after every three trials to make sure the magnetometer was always in a high-accuracy status during testing.

Prostate Phantom Study in CT Scanner

To validate the feasibility of the system in clinical environment, a prostate phantom with three lesions (CIRS Inc., Norfolk, VA), shown in Fig. 5, was used for testing in CT environment. The system and phantom were aligned through a laser and fixed on the CT table as shown in Fig. 6. Then a target tumor was randomly selected by a technician, and the distance between the needle tip and the tumor was measured on the CT monitor. Following the measurement, the needle was moved under the navigation of the tracking device to punch the tumor. Next, it was scanned again to verify the tracking error. After this, another tumor was randomly selected, and the procedures were repeated. In total, five tests were conducted in the phantom study.

RESULTS

Working Area

The working area was set to the right of the smartphone. Based on the measurement results, the effective working area with the mentioned magnet was 60 mm (width) × 80 mm (height) starting from the right edge of the smartphone. The SNR was less than 1.5 once the magnet was located outside of this area, which could lead to a large tracking error in a CT environment.

Open Air Test

The radial error distribution of the open-air test is shown in Fig. 7(a). The average radial error of the presented tracking method was calculated as 0.47 mm with 25 trials, and the standard deviation was 0.29. The maximum radial error was 0.98 mm, which was appeared in the right top corner of the platform. This position has the farthest distance from the smartphone, so the lowest SNR in the working area could cause a maximum error. Furthermore, the radial error was between − 0.58 and 0.75 mm based on the Bland–Altman plot with a 95% confidence interval, as shown in Fig. 7(b). Besides, we analyzed the error distribution

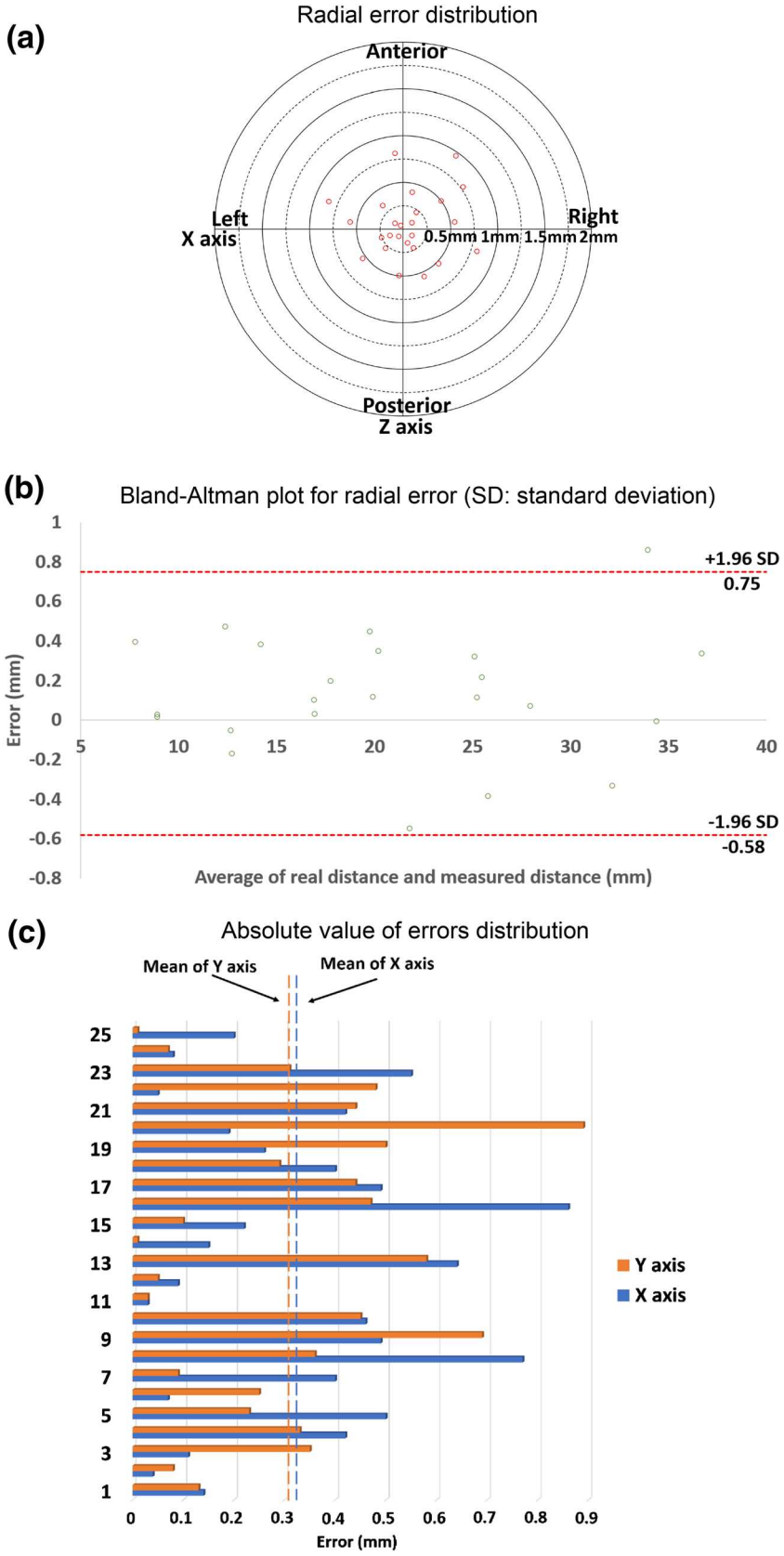

FIGURE 7. (a) Radial error distribution. (b) Bland-Altman plot of radial distance with 95% confidence interval. (c) The absolute value of errors distribution in *x*-axis and *y*-axis of CT coordinate system.

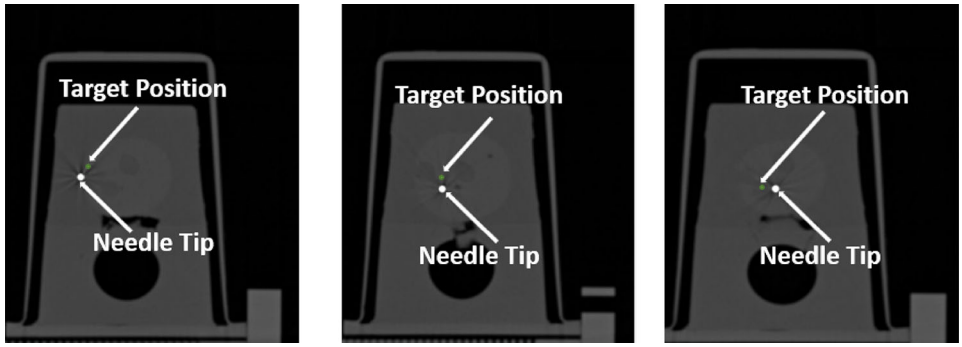

FIGURE 8. The CT images of prostate tests. White point: the position of inserted needle. Green point: position the target point. The distance between the target point and needle position is considered as radial error.

in the x-axis and y-axis of the CT coordinate system; Fig. 7(c) shows that the average errors were 0.32 and 0.30 mm, respectively. The maximum errors were 0.86 and 0.89 mm for the x-axis and y-axis of the CT coordinate system, respectively.

Prostate Phantom Test

In a CT environment, tumor targeting was conducted with a prostate phantom to prove the feasibility of the presented method. The radial error, left-right error, and anterior-posterior error for all five tests were measured. Figure 8 shows CT images of three trials. The average errors of the tracking device were 2.25, 1.30, and 1.71 mm for radial error, left-right error, and anterior-posterior error, respectively. The standard deviations were 1.63, 1.27, and 1.92 for radial error, left-right error, and anterior-posterior error, respectively.

The average error in the tumor targeting with the prostate phantom test was slightly higher than the average error conducted in the open-air test. This is due to tissue deformation and target shift during the needle insertion.

DISCUSSION

This study aimed to develop a low-cost method to assist with needle positioning before needle insertion in minimally invasive procedures. And the tests results of presented method show that it is feasible to use a permanent magnet and a smartphone for needle tracking before insertion, but several factors can still affect the accuracy.

First, the measurement accuracy of the magnetometer determines the tracking accuracy. Sometimes, especially when the magnet is too close to the magnetometer on the phone, there is some residual magnetism in the magnetometer. This can introduce an offset in the measured data. Therefore, it is helpful for the user to wave the smartphone in a figure-eight motion before each round of tracking to eliminate residual magnetism and thus improve the measurement accuracy of the magnetometer.[14]

Second, the SNR is very important to the tracking accuracy. Since the magnetic field of background environment is not stable and exhibits many slight changes, if the SNR is too small, these slight changes will have a major effect on the calculation of the magnetic field from the magnet, resulting in tracking error. To acquire better tracking results, the SNR must be greater than 1.5. If the SNR is less than 1.5, the error will increase significantly. One way to increase the SNR is to use an enormous magnet that can generate a stronger magnetic field.

In addition, the strength of the magnetic field decreases significantly with the increase of distance between the magnetometer and magnet, which leads to the decrease of the SNR and inaccurate tracking. Therefore, it is better for the working area to be as close as possible to the magnetometer in order to acquire higher SNR and better tracking accuracy. However, the working area should not be too close to the magnetometer in the phone. In this study, we applied the magnetic dipole model, which requires the distance between the magnet and magnetometer to be big enough to consider the magnet as a dipole. Usually, the distance should be bigger than three times the size of the magnet to apply the magnetic dipole model. Furthermore, putting the magnet too close to the magnetometer in the smartphone could cause residual magnetism and lead to a measurement offset of the magnetometer, which would decrease the tracking accuracy.

Third, improper placement of the smartphone and magnet on the operation platform could cause an error. Since the math model requires that the magnetic moment of the magnet (i.e., S–N axis) be in parallel with one axis of the magnetic sensor, the improper

placement of the smartphone could prevent the assumption of the math model from being satisfied. This could lead to the inaccurate measurement of the magnetic field strength in three axes, which could cause the navigation information to be incorrect. To acquire accurate navigation information, the operator should make sure that the smartphone and magnet are properly placed in the holders of the operation platform to satisfy the assumption of the math model.

Fourth, as a general problem of device tracking, patient motions could also cause navigation error, since the pre-acquired CT images are used to plan the trajectory of the needle. Once the position of the patient changes after CT scanning, the position of the needle tip relative to the target is also changed. One way to alleviate this problem is to attach a dynamic tracking reference to the patient. This could help to reduce the change of relative position caused by patient movement.

Furthermore, the cleaning and sterilization issues would need to be considered before applying the presented platform in a clinical interventional environment. The 3D printed platform can be sterilized through the normal process or the platform can be manufactured by sterilizable materials directly. Since magnetic fields can pass through non-metal material, the smartphone can be placed inside a transparent sterilized plastic bag to meet the cleaning and sterilization requirements.

In conclusion, we presented a smartphone-based permanent magnet tracking method for such purpose in this study. An operation platform with a needle insertion template, adjustable phone holder, and magnet holder was printed by a 3D printer. The test results show that the presented needle positioning method has an average radial error of 0.47 mm and 2.25 mm for an open-air test and a prostate phantom test in a CT environment, respectively. The presented design is portable and inexpensive. Furthermore, the proposed method is potentially comparable with existing template approaches as a cost-efficient alternative for certain procedures that can benefit from an assistive method for positioning a needle at a suitable entry point. In the future, an increase in the working area should be investigated. Also, *ex vivo* and *in vivo* tests will be conducted to verify the positioning performance of the presented method.

ACKNOWLEDGMENTS

This study was supported in part by the National Institutes of Health (NIH) Bench-to-Bedside Award, the NIH Center for Interventional Oncology Grant, the National Science Foundation (NSF) I-Corps Team Grant (1617340), NSF REU site program 1359095, the UGA-AU Inter-Institutional Seed Funding, the American Society for Quality Dr. Richard J. Schlesinger Grant, the PHS Grant UL1TR000454 from the Clinical and Translational Science Award Program, and the NIH National Center for Advancing Translational Sciences, the NIH Center for Interventional Oncology: Grant ZID# BC011242 & CL040015 and supported by the Intramural Research Program of the National Institutes of Health.

REFERENCES

[1]Abayazid, M., G. J. Vrooijink, S. Patil, R. Alterovitz, and S. Misra. Experimental evaluation of ultrasound-guided 3D needle steering in biological tissue. *Int. J. Comput. Assist. Radiol.* 9(6):931–939, 2014.

[2]Abdelnasser, H., A. Khalafallah, and M. Yousef. MagController: a system for touchless mobile devices control using the magnetic field. In: 2018 IEEE International Conference on Pervasive Computing and Communications Workshops (PerCom Workshops), IEEE, 2018, pp. 300–305.

[3]Abdelnasser, H., M. Youssef, and K. A. Harras. Magboard: magnetic-based ubiquitous homomorphic off-the-shelf keyboard. In: 2016 13th Annual IEEE International Conference on Sensing, Communication, and Networking (SECON), IEEE, 2016, pp. 1–9.

[4]Abe, T., B. Shizuki, and J. Tanaka. Input techniques to the surface around a smartphone using a magnet attached on a stylus. In: Proceedings of the 2016 CHI Conference Extended Abstracts on Human Factors in Computing Systems, ACM, 2016, pp. 2395–2402.

[5]Black, P. M., T. Moriarty, E. Alexander, P. Stieg, E. J. Woodard, P. L. Gleason, C. H. Martin, R. Kikinis, R. B. Schwartz, and F. A. Jokesz. Development and implementation of intraoperative magnetic resonance imaging and its neurosurgical applications. *Neurosurgery* 41(4):831–845, 1997.

[6]Chen, K.-Y., K. Lyons, S. White, and S. Patel. uTrack: 3D input using two magnetic sensors. In: Proceedings of the 26th Annual ACM Symposium on User Interface Software and Technology, ACM, 2013, pp. 237–244.

[7]Cheung, V., and A. Girouard. Exploring around-device tangible interactions for mobile devices with a magnetic ring. In: Proceedings of the Twelfth International Conference on Tangible, Embedded, and Embodied Interaction, ACM, 2018, pp. 108–114.

[8]Chow, T. L. Introduction to Electromagnetic Theory: A Modern Perspective. Burlington: Jones & Bartlett Learning, 2006.

[9]Civco. Disposable Template Grids. Civco Medical Solutions.

[10]Franz, A. M., T. Haidegger, W. Birkfellner, K. Cleary, T. M. Peters, and L. Maier-Hein. Electromagnetic tracking in medicine—a review of technology, validation, and applications. *IEEE Trans. Med. Imaging* 33(8):1702–1725, 2014.

[11]Gergel, I., J. Hering, R. Tetzlaff, H. P. Meinzer, and I. Wegner. An electromagnetic navigation system for trans-

bronchial interventions with a novel approach to respiratory motion compensation. *Med. Phys.* 38(12):6742–6753, 2011.
[12]Han, X., H. Seki, Y. Kamiya, and M. Hikizu. Wearable handwriting input device using magnetic field: geomagnetism cancellation in position calculation. *Precis. Eng.* 33(1):37–43, 2009.
[13]Henken, K. R., J. Dankelman, J. J. van den Dobbelsteen, L. K. Cheng, and M. S. van der Heiden. Error analysis of FBG-based shape sensors for medical needle tracking. *IEEE/ASME Trans. Mechatron.* 19(5):1523–1531, 2014.
[14]Hwang, S., M. Ahn, and K.-Y. Wohn. MagGetz: customizable passive tangible controllers on and around conventional mobile devices. In: Proceedings of the 26th Annual ACM Symposium on User Interface Software and Technology, ACM, 2013, pp. 411–416.
[15]Kelly, A. A 3D state space formulation of a navigation Kalman filter for autonomous vehicles. Pittsburgh PA: Carnegie Mellon University, Robotics Institute, 1994.
[16]Kochavi, E., D. Goldsher, and H. Azhari. Method for rapid MRI needle tracking. *Magn. Reson. Med.* 51(5):1083–1087, 2004.
[17]Krücker, J., S. Xu, N. Glossop, A. Viswanathan, J. Borgert, and H. Schulz. Electromagnetic tracking for thermal ablation and biopsy guidance: clinical evaluation of spatial accuracy. *J. Vasc. Interv. Radiol.* 18(9):1141–1150, 2007.
[18]Li, R., S. Xu, I. Bakhutashvili, I. B. Turkbey, P. Choyke, P. Pinto, B. Wood, and T. H. Zion. Template for MR visualization and needle targeting. *Ann. Biomed. Eng.* 47(2):524–536, 2019.
[19]Pourtaherian, A., S. Zinger, P. de With, H. H. Korsten, and N. Mihajlovic. Gabor-based needle detection and tracking in three-dimensional ultrasound data volumes. In: 2014 IEEE International Conference on Image Processing (ICIP), IEEE, 2014, pp. 3602–3606.
[20]Reid, I., and H. Term. Estimation II. www.robots.ox.ac.uk. Oxford University. Retrieved 6 August 2014.
[21]Tilak, G., K. Tuncali, S. E. Song, J. Tokuda, O. Olubiyi, F. Fennessy, A. Fedorov, T. Penzkofer, C. Tempany, and N. Hata. 3T MR-guided in-bore transperineal prostate biopsy: a comparison of robotic and manual needle-guidance templates. *J. Magn. Reason. Imaging* 42(1):63–71, 2015.
[22]Tokuda, J., K. Tuncali, I. Iordachita, S. Song, A. Fedorov, S. Oguro, A. Lassó, F. Fennessy, Y. Tang, C. Tempany, and N. Hata. Preliminary accuracy evaluation of 3T MRI-guided transperineal prostate biopsy with grid template. In: 19th Annual Meeting and Exhibition, International Society of Magnetic Resonance in Medicine. Proceedings of the International Society for Magnetic Resonance in Medicine, 2011, vol. 19, p. 3761.
[23]Vrooijink, G. J., M. Abayazid, and S. Misra, Real-time three-dimensional flexible needle tracking using two-dimensional ultrasound. In: 2013 IEEE International Conference on Robotics and Automation (ICRA), IEEE, 2013, pp. 1688–1693IEEE.
[24]Yoon, S. H., K. Huo, and K. Ramani. TMotion: embedded 3D mobile input using magnetic sensing technique. In: Proceedings of the TEI'16: Tenth International Conference on Tangible, Embedded, and Embodied Interaction, ACM, 2016, pp. 21–29.
[25]Zhao, Z, Z. T. Tse. A smartphone and permanent magnet-based needle guidance system. In: 2019 International Symposium on Medical Robotics (ISMR), IEEE, 3 Apr 2019, pp. 1–5.